Lucy L'Ralph In-Flight Calibration and Results at (152830) Dinkinesh

Amy A. Simon[1], Hannah H. Kaplan[1], Dennis C. Reuter[1], Matthew Montanaro[2], William M. Grundy[3], Allen W. Lunsford[4], Gerald E. Weigle[5], Richard P. Binzel[6], Joshua Emery[7], Jessica Sunshine[8], Carly Howett[9], Hal Levison[10], Simone Marchi[9], Keith S. Noll[1], John Spencer[9]

Abstract

The L'Ralph instrument is a key component of NASA's Lucy mission, intended to provide spectral image data of multiple Jupiter Trojans. The instrument operates from ~0.35 to 4 μm using two focal plane assemblies: a 350 to 950-nm multispectral imager, MVIC, and an 0.97 to 4-μm imaging spectrometer, LEISA. Instrument calibration was established through ground testing before launch and has been monitored during cruise utilizing internal calibration sources and stellar targets. In-flight data have shown that the instrument thermal performance is exceeding expectations, allowing for early updates to LEISA radiometric and pointing calibrations. MVIC radiometric performance remains stable more than three years since launch. The serendipitous identification of a new flyby target, (152830) Dinkinesh, allowed testing of instrument performance and interleaved LEISA and MVIC acquisitions on an asteroid target. Both MVIC and LEISA obtained data of Dinkinesh and its moon, Selam, demonstrating that they show good spectral agreement with an S or Sq-type asteroid, along with evidence of a 3-μm absorption feature.

[1] NASA Goddard Space Flight Center, Solar System Exploration Division, Greenbelt, MD 20771, USA. Corresponding author email: amy.simon@nasa.gov
[2] Rochester Institute of Technology, Carlson Center for Imaging Science, Rochester, NY 14623, USA
[3] Lowell Observatory, Flagstaff, AZ 86001, USA
[4] American University, Physics Department, NW Washington, DC 20016, USA
[5] Big Head Endian, Winfield, KS 67156, USA
[6] Massachusetts Institute of Technology, Department of Earth, Atmospheric and Planetary Sciences, Cambridge, MA 02139 USA
[7] Northern Arizona University, Dept. of Astronomy and Planetary Science, Flagstaff, AZ 86011, USA
[8] University of Maryland, Department of Astronomy and Department of Geology, College Park, MD 20742 USA
[9] Planetary Science Institute, 1700 East Fort Lowell, Suite 106, Tucson, AZ 85719, USA and Atmospheric, Oceanic and Planetary Physics, University of Oxford, Clarendon Labs, Parks Road, Oxford, OX1 3PU, UK
[10] Southwest Research Institute, Boulder CO 80302 USA

1. Introduction

Lucy is a NASA Discovery-class mission that launched in 2021 to investigate a previously unexplored class of bodies, the Jupiter Trojan asteroids. Lucy will fly past a number of these objects, visiting the Jupiter-leading L4 swarm in 2027 and the trailing L5 swarm in 2033 (H. Levison et al. 2021; C. Olkin et al. 2024). A major goal of the mission is to visit multiple Trojan asteroids with different spectral types to understand the compositional diversity of these bodies and their implications for solar system formation (C. Olkin et al. 2021). As these bodies are at 5 AU, and the flyby geometries vary, the Lucy instruments were designed to operate under low illumination conditions with science requirements to observe effective surface brightness (intensity divided by incident solar flux, *I/F*) from as low as 0.0014 (visible) to 0.0019 (IR) to as high as 0.4 (both spectral regions) (D. Reuter et al. 2023).

The Lucy L'Ralph instrument is two instruments in one: a multi-channel visible to near-infrared wavelength imager and a shortwave IR imaging spectrometer (D. Reuter et al. 2023). It draws on heritage from the New Horizons Ralph and the OSIRIS-REx OVIRS instruments (D. Reuter et al. 2008; D. Reuter et al. 2018). The Multi-spectral Visible Imaging Camera (MVIC) uses time-delay integration (TDI) across six separate 5024x64 pixel CCDs on a single substrate to construct images with spatial instantaneous field of view (iFOV) of ~29 μrad pixel^{-1}. Filters over each CCD define the wavelength ranges of the six channels: the panchromatic (pan, Band 1: 350 – 950 nm), violet (Band 2: 375 – 480 nm), green (Band 3: 480 – 520 nm), orange (Band 4: 520 – 625 nm), phyllosilicate (Band 5: 625 – 750 nm), and near-infrared (Band 6: 750 – 950 nm). The Linear Etalon Imaging Spectral Array (LEISA) operates from 0.97 to 4.01 μm using three linear variable filters (LVFs), with overlapping wavelengths, mounted above 1024x1472 pixels of a 2048x2048 HgCdTe infrared detector (H2RG), with an iFOV of ~40 μrad pixel^{-1} (D. Reuter et al. 2023). The LEISA effective wavelength varies with row down the array, as well as changing a small amount in the cross-track direction due to filter smile (Figure 1).

The MVIC CCDs span a total of ~145 mrad in the cross-track and ~16 mrad in the TDI/along-track direction, with 0.9 mrad spacing between CCDs. The LEISA array spans ~41 mrad in the cross-track and ~60 mrad in the spectral/along-track direction (Figure 1). Both detectors share the same optical path, and an internal scan mirror is used to build up image cubes of the target (Figure 1) and can scan ± 4° (± 70 mrad) on the sky in the along-track direction. Because LEISA uses an IR sensor, the focal plane assembly (FPA) must be passively cooled to reduce the background dark current (R. Blank et al. 2012); nominal LEISA FPA operating temperature is between 95 and 105 K, though it was calibrated over a range of 90 to 117 K. Nominal thermal conditions for the MVIC FPA are ~150 to 200K, though it can operate at ambient temperatures. The instrument design and operation are described further in D. Reuter et al. (2023).

L'Ralph development followed a standard integration and test campaign that included performance verification tests to show the instrument would achieve its science requirements. This campaign was composed of multiple smaller campaigns that included ambient testing for MVIC and thermal vacuum cryogenic testing for both MVIC and LEISA. This paper describes the ground test campaigns and their limitations in Section 2. In Section 3 we will discuss the in-flight calibration campaigns and their results. Section 4 will demonstrate the performance verification conducted during the 152830 Dinkinesh flyby in November 2023. Section 5 compares the Dinkinesh spectral data with that of other asteroids and ordinary chondrites. We conclude with upcoming calibrations in anticipation of the first Trojan asteroid flybys in 2027.

2. Ground Calibration Campaign

Instrument integration and testing occurred primarily in 2020 and was hampered by the global pandemic. As such, the testing was performed under very different conditions and restrictions than usual: testing teams were smaller, facilities were not operating at full capacity, finding or ordering needed equipment was challenging, and special care had to

be taken to avoid illness while balancing constrained schedules (M. Garrison et al. 2022). To best optimize the testing time, experienced individuals were brought on from previous instrument calibration campaigns and the testing was planned in detail before execution. The calibration team utilized three 8-hour shifts, with overlap time, to minimize the downtime during testing.

For thermal vacuum (TVac) testing, we utilized calibration ground support equipment (calGSE) that was developed for use on previous IR instruments and expanded for visible wavelength coverage for OSIRIS-REx OVIRS (M. Montanaro et al. 2014; A. Simon et al. 2018; A. Simon et al. 2021). This large, liquid-nitrogen cooled, system can be pushed into the thermal vacuum chamber with the instrument for radiometric, geometric, spectral, and pointing calibrations and is described in detail in D. Reuter et al. (2023). TVac was split into two campaigns each covering multiple thermal cycles, with vibration tests in between. One difficulty with L'Ralph testing is that while additional testing can be run for MVIC under ambient conditions, LEISA performance can only be checked under cryogenic temperatures.

The calGSE uses several sources to cover the full spectral range of L'Ralph. At short wavelengths, the calGSE uses a variable-attenuation, fiber optic-fed, visible integrating sphere (VIS) coated with a Spectraflect lining (Labsphere 2017). Prior to use, the VIS was calibrated for single fiber use at various attenuation levels and covering the spectral range from 250 to 2500 nm. The radiometric uncertainty was $\leq 1\%$ between 450 and 2300 nm. For infrared wavelengths, the calGSE includes a wide aperture IR Flood source that can be operated at blackbody temperatures from 180 to 360K. The IR source is National Institute of Standards and Technology (NIST) calibrated to better than 0.2%, confirmed prior to TVac (A. Pearlman et al. 2020). Additional sources were used to confirm pointing, pixel point spread functions, and spectral calibration (D. Reuter et al. 2023).

Despite the available calibration equipment, there were still challenges in replicating the deep space environment in the chamber, which led to several calibration uncertainties. First, the large amount of equipment in the chamber meant that, even with blankets and light shields, non-flight-like glints and reflections can cause apparent scattered light features. These scattered light features were especially problematic for MVIC with its very wide field of view. Next, although the calGSE does include steerable small sources for pointing verification, L'Ralph includes an internal along-track scan mirror, and the instrument itself is mounted on a moving platform on the spacecraft, so a pointing vector must account for all three factors. Thermal effects added uncertainty to the TVac pointing vector measurements: the calGSE has a known pointing shift (in the L'Ralph along track direction) from ambient metrology as it transitions to cryogenic temperatures (adds up to 2 mrad uncertainty) and we noted a thermal pointing shift internal to L'Ralph (up to 0.45 mrad over a 30K change), as well. These uncertainties have a bigger effect on LEISA than MVIC because of its larger along track field of view.

Lastly, LEISA is dependent on a combination of the VIS and the IR Flood sources for accurate radiometric calibration in the 2 to 3-μm range, where important spectral features occur, but also where the signal falls off rapidly from both calibration sources. Additionally, with a notional detector cutoff (50% response) of 3.95 μm, the LEISA detector has lower IR sensitivity when it is warm (e.g., R. Blank et al. 2012). At IR Flood source temperatures > 270K, the LEISA detector saturated at longest wavelengths and, when the detector was cold, it also showed evidence of out-of-band signal at these important wavelengths (infrared photons leaking into shorter wavelength regions). This out-of-band signal is dependent on the source IR brightness and spectral shape, as well as the detector temperature-dependent response, and is common in these broad linear variable filters (A. Simon et al. 2021). However, out-of-band signal will not pose a problem for Lucy's cold Main Belt and Trojan targets, as they will have few photons near 4 μm.

An additional calGSE issue was discovered during testing that mainly affected LEISA radiometric calibration. The electrical currents recorded from the VIS source during radiometric testing showed a discrepancy with pre-TVac calibration; these currents are used to convert the VIS output to known radiance levels and were above the values expected. After testing concluded, the chamber configuration was dismantled, and it was noted that the baffle on the critical variable-attenuation VIS fiber was out of alignment. During testing this would result in some light exiting the VIS with fewer surface reflections and causing non-uniformity recorded as larger measured current values. This misalignment most affects calibration for wavelengths > ~1100 nm, where the Spectraflect lining reflectance curves differ the most from the Spectralon baffle surface (LabSphere 2017). As the vendor calibration curves were based on an integrated power response across all wavelengths, we expected an in-flight calibration correction would be needed, particularly to LEISA performance below ~2.6 μm.

3. In-flight calibration

3.1 LEISA

LEISA was expected to be too warm for routine operations until after the spacecraft passes beyond 3 AU from the Sun (D. Reuter et al. 2023). However, pointing the instrument radiator away from the spacecraft solar arrays does allow the focal plane to cool sufficiently to obtain useable signal, even above the maximum calibrated temperature (117 K). LEISA operation was first tested during the October 2022 Earth gravity assist. At 150 K, the detector was well above its nominal operational temperature, but valid spectral data were collected at some wavelengths (D. Reuter et al. 2023; J. Spencer et al. 2024). Subsequently, several tests and updated thermal models showed that LEISA could achieve its nominal operational temperatures at 2 AU, if allowed to pre-cool before science observations.

The ability to pre-cool LEISA to operational levels was tested in July 2023 with a series of Arcturus stellar scans. In this campaign, the instrument pointing platform was off pointed, allowing LEISA to cool to ~110K, well within its nominal range. Using five separate cross track positions on LEISA, the L'Ralph mirror scanned from dark space across the star and back to dark space, effectively moving Arcturus along the LEISA filters in the spectral direction from red to blue wavelengths. Several things were noted in the scans: 1) the star did not cross the entire focal plane, 2) the star was scanned to move 1.5 pixels per integration, but the motion did not align with what was observed, with about a 2% difference, and 3) the calibration radiances for Arcturus were lower than reference values from 1.1 to 2.5 μm, as expected. Failure to scan the star across the entire focal plane (it stopped at about 1.1 μm, ~50 pixels from the detector end), would indicate either an offset in the pointing vector or incorrect scan length parameters were used. However, the concurrent mismatch in star position and scan rate would mean that the scan mirror did not scan as commanded, or the pixel angular size was incorrect.

The LEISA stellar scans were repeated in March 2024, offsetting the scan rate by 2% and the pointing by 1.6 mrad. In these new scans, the star tracked exactly one pixel per frame, confirming that the scan rate was now correct. However, the scan still stopped short of the end of the LEISA filters, by about 10 pixels, indicating that the scan length was incorrect. Fixed pointing checks were also run against the LORRI camera with fixed positions rather than scans to confirm relative pointing knowledge, as well as confirming the LEISA full width half maximum (FWHM) of the point spread function (PSF) as ~2 pixels. The combined tests proved that the pixel iFOV (and scan length) should be adjusted by 2%, from the TVac-derived rough angular size of 40 ± 3 μrad per pixel to 40.75 ± 0.05 μrad per pixel. The LEISA pointing vector was also updated by 1.8 mrad relative to the internal scan mirror zero position.

For the radiance calibration, the flux from Arcturus was summed over 9x9 pixels for each wavelength, to account for the full extent of the PSF, as LEISA calibration was defined for

extended sources. The summed values were converted to radiance using the TVac-derived calibration coefficients and then compared with a reference Arcturus spectrum (J. Rayner et al. 2009) convolved to the LEISA spectral resolution. The ratio of the measured to reference spectrum was found at each cross-track position that was scanned and interpolated across the entire LEISA field of view. The ratio of expected to measured radiance was ~1.01 at 1.1 μm, to a maximum of ~1.8 near 2.1 to 2.2 μm (Figure 2). The in-flight calibration below ~1.0 μm is not yet verified, as we do not have LEISA stellar data at these wavelengths.

A last effect to note for LEISA is optical fringing. During TVAC testing, some observations showed evidence of a repeating brightness variation, particularly at low light levels. This effect is seen in the Arcturus stellar scans, as well as in internal calibration source data (Figure 3). Although antireflective coatings are applied to all surfaces, optical modeling shows the likely cause is a reflection off the detector to the back of the filters and back to the detector. The effect can be mitigated by creating fringe flats that can be applied after the data are calibrated.

Currently, fringe flats are created using the data itself for each observation. For the internal sources (Figure 3), the full frame was already illuminated, but for a smaller object, such as an asteroid, a master frame was constructed that sums together the source illumination as it moved across the field of view (in effect, a “smeared” flat). Single pixel artifacts were removed, and 2D median filters were applied to smooth the data in each filter. Next, a sliding Gaussian was iteratively fit, row-by-row and across each filter, and a local mean background level was calculated across multiple fringes. The resulting fringe flat was constructed by dividing the Gaussian model at each fringe by the local mean background. Attempts are underway to determine if the fringe pattern can be more accurately modeled from optical properties for better removal, but the current method does significantly reduce the fringes from up to 20% of the brightness value to a few percent or better. These team-derived Dinkinesh flats, and their documentation, were delivered with the calibrated

data to the Planetary Data System (PDS) for post-calibration processing by end users (D. Reuter et al. 2024a).

3.2 MVIC

MVIC operates at higher temperatures than LEISA, which has allowed for more extensive in-flight calibration while the spacecraft is in the inner Solar System. Calibration data were taken of the Earth and Moon during Lucy's first Earth gravity assist (EGA-1), each acquired at five cross track positions. Other routine calibrations were completed on multiple occasions: May 2022 (0.97 AU), March 2023 (1.74 AU), and March 2024 (2.02 AU). At each opportunity, radiometric stability was checked with an internal filament source, a solar calibration, and with observations of three different star clusters, M6 (Butterfly Cluster, NGC6405), M7 (NGC 6475) and the Wishing Well (NGC 3532). M6/M7 and Wishing Well are each scanned at five cross track positions to assess variation across the detector; pointing is repeated between each calibration opportunity leading to comparable image sets from each of our routine calibrations.

Early analysis demonstrated MVIC performance conforms with expectations from TVac testing and meets or exceeds mission requirements. The PSF does not vary across the detector and, with a FWHM of ~1.7 pixels (50 μrad), is consistent with requirements (D. Reuter et al. 2023). Lunar data from EGA-1 show good agreement with RObotic Lunar Observatory (ROLO) standard modeled data and with Moon Mineralogy Mapper hyperspectral images over the same lunar surface regions (D. Reuter et al. 2023), demonstrating that the radiometric calibration coefficients derived from TVac data are accurately calibrating data in all bands from counts to radiance. We were also able to show that the signal from scattering is <<1% for the angular range of observations pertinent to the Trojan encounters using the saturated EGA-1 Earth observations (D. Reuter et al. 2023).

Since the initial in-flight calibration results reported in D. Reuter et al. (2023), we have continued performance trending. The MVIC FPA temperature was 212 K in May 2022, 156 K in March 2023, and 160 K in March 2024; we use TVac data taken at 152 K for comparison. Internal filament calibration data taken at similar temperature (TVac, March 2023, March 2024) shows better agreement than for the early higher temperature data (May 2022), which are offset from the rest as the instrument electronics and focal planes has not yet reached nominal flight temperatures. Fractional bias is ± 2% for each of 5024 pixels across the detector in panchromatic, orange, phyllo, and NIR channels. The shortest visible channels, violet and green, have much higher fractional bias because they have very low signal (<100 counts over background), but otherwise show the expected agreement.

For the stellar calibrations, we used astrometry to find the celestial coordinates of each image to co-register images from the three calibration opportunities (May 2022, March 2023, March 2024). We then identified 400 stars that can be found in all three observations. Data are converted to calibrated radiance using calibration coefficients that were derived from TVac and tested on the Moon EGA-1 data. We find the center pixel for each star and sum over a 5x5 pixel area to account for the full extent of the PSF. When data from all three calibration opportunities are compared, there is ±5% agreement in radiance for the same star at similar positions across datasets (Figure 4). As with the internal calibration data, agreement is best between the March 2023 and 2024 datasets taken at similar MVIC and electronics temperatures. Although MVIC was intended for extended rather than point sources, these stellar calibrations place an upper limit on radiometric uncertainty. When stars are tracked at multiple positions across the detector, radiance values are also ±5%, indicating consistent calibration across the detectors.

4. Dinkinesh flyby

On 1 November 2023, Lucy encountered Main Belt asteroid (152830) Dinkinesh, which was added to the mission to provide an earlier opportunity to test flyby target tracking and

science operations (H. Levison et al. 2024). Although the encounter occurred at 2.26 AU, it was again hoped that LEISA could be pre-cooled to allow for unsaturated data. Due to flyby constraints on pointing and timing, optimal LEISA pre-cooling was limited, but the FPA cooled to 119 K, just above the calibrated operating range. The two focal planes cannot be commanded at the same time, and require different scan parameters, so this flyby also tested the ability to interleave LEISA and MVIC observations (D. Reuter et al. 2024a; 2024b). For each focal plane, three scans were conducted around closest approach (C/A) with varying range and phase angles (Table 1).

As the Lucy system tracking performance was not yet characterized, the scans were padded for significant uncertainty in pointing positions. Both LEISA and MVIC conducted three target scans and used short exposure times as Dinkinesh is more reflective and closer to the Sun than the Trojan targets for which the instrument is optimized. For the LEISA scans, the exact pointing and scan rate were still in question at the time of Dinkinesh planning. To adjust for the limited knowledge, and to keep the scan length reasonable, we scanned at a rate equivalent to ~1.55 (assuming 40-μrad per pixel) pixels per frame with integration times of 70 to 80 ms per frame, Table 1. This scan rate accounted for the 2%-pixel size/scan rate issue identified in the July 2023 stellar calibrations, while keeping Dinkinesh within the extended point spread function of a pixel. Dinkinesh's satellite, Selam, was unknown at the time of planning (H. Levison et al. 2024), but other flyby aspects, such as changing phase angle and range during observations, were included in the planning process.

While MVIC can only be scanned across the object in the TDI (positive scan) direction, LEISA can be scanned in either direction. The first LEISA observation was conducted scanning from short to long wavelengths, while the other two scanned from long to short wavelengths. The scan direction primarily matters during the period of rapidly changing phase angles near closest approach, when the shorter wavelengths may saturate but the longer wavelengths can benefit from increased illumination at lower phase angles (see

Table 1 and Figure 5). Figure 5 also shows an individual frame from the LEISA C/A scan, as well as the panchromatic (Band 1) C/A image from MVIC.

During the flyby, MVIC collected data with its shortest possible integration time (7.2 ms per TDI line). Because of the pointing margin, the MVIC datasets cover ~1500 pixels in the along-track direction even though Dinkinesh only spans ~50 MVIC pixels at C/A. Dinkinesh and Selam are well-exposed in all channels and images except for a small number of saturated pixels in the C/A image panchromatic channel. Calibrated radiance was converted to *I/F* by dividing by the CALSPEC solar flux (R. Bohlin et al. 2014) integrated over the MVIC band passes and scaled to Dinkinesh's solar distance (Figure 6a). There is a 96-pixel offset between each MVIC channel in a scan (64 pixels per detector plus 32-pixel space between detectors). Each channel is shifted by the appropriate offset to align the six bands so that spatially related pixels are aligned; limb data do not match exactly due to the changing viewing conditions and target size within the dataset.

Using disk-averaged spectra from the three MVIC scans, we calculate a phase curve and find ~0.029 mag per degree change related to phase angle. Because of the fast scan rate and the timing of the images, MVIC does not see significant phase change within a dataset; there is a 2° phase change between the leading channel (pan) and trailing channel (NIR) in the C/A image and a <1° change in the Approach and Departure images (Table 1). The phase curve for each band is assessed individually and there is ~0.009 mag per degree difference between the reddest and bluest portion of the MVIC spectrum. As Dinkinesh and Selam spanned only a small number of illuminated pixels, we focused on analyzing the C/A and Departure scans to generate spectra for comparisons. We used the average 0.029 magnitude per degree change to correct all spectra to a 30° viewing geometry (Figure 6b).

LEISA spectrum construction is a bit more complex. As each LEISA along-track pixel is a different wavelength, spectrum generation requires tracking a surface area across each frame of the scan. To simplify this process, image cubes can be constructed for Dinkinesh

and Selam from each scan by taking each column of each LEISA frame, corresponding to a distinct wavelength, and re-projecting it to the corresponding wavelength layer of an output cube. For our analysis, the re-projection was to the apparent sky plane at the time of each frame, centered on the target, and accounting for target size changes during the scan. We did not account for the changing sub-spacecraft longitude and latitude on the target, nor were the data projected onto a shape model, limiting our ability to look for spectral variations on Dinkinesh's surface. Additionally, we did not model nor remove any thermal tail from the data as the Dinkinesh radiances show no evidence of thermal emission. This is not surprising, since at 2.3 AU the LEISA signal is dominated by reflected solar radiation for objects colder than ~250 K, even at low *I/F*, and all of our spectra are disk-averaged, including regions much cooler than the sub-solar point.

The LEISA data were converted to *I/F* using the CALSPEC solar flux (R. Bohlin et al. 2014) convolved over the LEISA band passes and scaled to 2.26 AU. The LEISA spectra were then generated by averaging over the illuminated pixels at each wavelength in each cube and then removing outliers two standard deviations from the mean and along filter boundaries (Figure 6c). We applied conservative ±7% error bars on the *I/F*, from the root mean square of 5% uncertainty from the LEISA radiance and an assumed 5% uncertainty from the solar flux. Selam and Dinkinesh are spectrally similar, as expected if they share a similar origin (H. Levison et al. 2024). However, the brightness of the two bodies cannot be directly compared as phase angle changed throughout the observations, particularly at closest approach; that is, Selam crossed the same spectral element at higher phase angles than Dinkinesh, and in some scans, did not cross all wavelengths.

The LEISA Departure scan occurred when Dinkinesh was at a higher phase angle than the C/A scan (Table 1), but it did not change as significantly throughout the observation, only ~3°. To determine the Dinkinesh near-IR phase curve, we found the value that resulted in the best match between the two Dinkinesh scans when corrected to the phase angle at end of the C/A scan (~30°). This resulted in a best fit photometric phase correction of

0.0316 magnitude per degree with a $\chi^2 = 0.41$, ignoring any possible phase reddening or other surface parameters. A best fit phase reddening was found by comparing the phase angle of the two scans and spectral slope between 1.1 and 3.7 μm. With so many parameters simultaneously changing during the scans and the reduced long wavelength sensitivity, the uncertainties are large, but we find a best-fit phase reddening *I/F* slope change of ~0.0002 per μm per degree (Figure 6d). No other surface parameters (i.e., roughness) could be reliably fit due to the changing object geometry and illumination in these limited scans.

5. Discussion

Visible and near-infrared spectra of the Dinkinesh system from the Keck and Gemini observatories show a red (i.e., positively increasing) spectrum from 0.45 to 0.8 μm and an absorption band centered near 1 μm (B. Bolin et al. 2023). These observations predicted that Dinkinesh is an S- or Sq-type asteroid. The phase-corrected, disk-averaged, MVIC spectra show increasing reflectance with wavelength that flattens in the NIR channel (Figure 6b). The NIR filter subtends part of the 1-μm absorption feature typical of S-type asteroids as indicated by the spectral flattening, but the effective wavelength of NIR is ~0.75 μm, which is too short to show a more significant downturn from a 1-μm absorption feature.

We also performed an initial analysis of spatial color variation on Dinkinesh using all channels in the MVIC closest approach image which had a spatial resolution of ~14 m per pixel. Given Dinkinesh's small size in our scans, MVIC would be more likely to show spatial variation than LEISA, which had a best spatial resolution of ~25 to 35 m per pixel near closest approach. To first order, there is little variation in any channel or channel ratio across the surface. However, neither the LEISA nor MVIC image cubes have been registered to a shape model, and therefore an individual pixel's ground location and phase angle may

not be accurate across bands or spectral channels. Instead, we focus on full-disk spectral comparisons with other S-complex asteroids.

To better compare the spectral type of Dinkinesh, we combined the MVIC and LEISA data to obtain a complete spectrum from 0.4 to 3.7 μm. For each focal plane, the Departure scan data were corrected to 30° phase with their respective phase curves (Figure 7a), as these data had fewer uncertainties from varying phase angle during the LEISA scan. The Dinkinesh spectrum has a clear 2-μm absorption band, the suggestion of the 1-μm band (Figure 7b), and a possible absorption near 3 μm (Figure 7c). From 0.4 to 2.5 μm, Dinkinesh's spectrum shows a reasonable spectral shape for an S-complex asteroid, for example, (433) Eros, (25143) Itokawa, (65803) Didymos, and (1036) Ganymed (R. Binzel et al. 2001, 2004; L. McGraw et al. 2022; D. Polishook et al. 2023). Note that the Dinkinesh 1-μm band depth is highly uncertain, as the LEISA calibration near these wavelengths needs to be repeated, as discussed in Section 3.1.

The S-complex asteroids' 1 and 2-μm absorption bands are due to pyroxene and are common in stony meteorites; S-complex subtypes are distinguished by the varying depth and central wavelength of the 1 and 2-μm absorption bands, as well as spectral slopes. (Figure 7b). Dinkinesh's 2-μm band is centered near 1.95 μm with a depth of ~6% and FWHM of ~0.45 μm. Unfortunately, the parameters of the 2-μm band alone cannot generally be used to assess the pyroxene chemistry or determine analog asteroid or meteorite sub-types. We therefore turned to direct spectral comparisons (i.e., curve matching), between the LEISA spectra of Dinkinesh and published spectra of ordinary chondrite meteorites (T. Dunn et al. 2010) and S-complex near-Earth and Main Belt asteroids (L. McGraw et al. 2022; M. McAdam et al. 2024).

Curves were compared after dividing out a spectral slope, computed as the best-fit line of each spectrum from 1.2 to 2.45 μm. Although S-complex asteroids show a continuum of 1 and 2-μm band centers, several provide good matches to L, LL, and H-chondrite

meteorites, for example (6) Hebe (H), (20) Massalia (L), and (15) Eunomia (LL) (R. Binzel et al 2019; M. Marsset et al. 2024). The MIT-Hawaii Near-Earth Object Spectroscopic Survey (MITHNEOS) spectra of these asteroids compare well with Dinkinesh's 2-μm band, particularly for Massalia and Eunomia (R. Binzel et al. 2019) (Figure 8a). In the meteorite collection, the average LL- and L-chondrite meteorites provide better matches to Dinkinesh than H-chondrites (Figure 8b). The poorer fits of the H-chondrites are mostly due to the peak near 1.5 μm (i.e., between the two absorption bands) being at a shorter wavelength than in the other ordinary chondrites. The H-chondrite 2-μm band center also tends to be at a shorter wavelength than in Dinkinesh.

We also computed the location of the ~1.5-μm peak and 2-μm band center in the spectra of the meteorites and Dinkinesh (Table 2 and Figure 9). The ordinary chondrite meteorites cluster by sub-type in the parameter space of 1.5-μm peak center vs 2-μm band center similarly to how they cluster in 1-μm band center vs 2-μm band center (T. Dunn et al. 2010). The similar clustering makes sense, in that the location of the 1.5-μm peak is set by the locations of the two absorption bands that bound it, so is heavily influenced by the 1-μm band. As such, even though we are not able to directly measure the 1-μm band center in the Dinkinesh spectra, we can use the 1.5-μm peak as a proxy in terms of meteorite comparisons. The measured band parameters of Dinkinesh suggest it is mineralogically similar to LL/L-chondrites, but it is not consistent with H-chondrite spectra. LL/L chondrites have the highest olivine content among ordinary chondrite meteorite classes (e.g., H. McSween et al. 1991) consistent with Dinkinesh's location in the inner Main Asteroid belt (e.g., P. Vernazza et al. 2014; E. Cloutis et al. 2015)

Lastly, Dinkinesh's 3.1-μm band has an apparent depth of ~6% (Figure 7c). However, we note that LEISA was operating outside of its designed calibration range and temperature effects are non-linear. We therefore urge caution in interpreting these longer wavelengths. We consider it likely that an absorption is present, but the accuracy of the depth and shape cannot be verified without other observations, including validation of any small thermal

emission. Absorptions in this wavelength range are generally associated with hydration, so it may seem unexpected to see such an absorption on an S-complex asteroid. However, 3-μm bands have been detected on a number of other nominally anhydrous bodies including the Moon (e.g., C. Pieters, et al., 2009; J. Sunshine et al. 2009), (4) Vesta (M. De Sanctis et al. 2012), near-Earth asteroids (NEAs; A. Rivkin et al. 2018; L. McGraw et al. 2022, 2024), L-type Main Belt asteroids (MBAs; J. Gomez Barrientos et al. 2024), and S-complex MBAs (M. McAdam et al. 2024). Hydration on these bodies has been attributed to interactions with the solar wind and/or physical contamination from impacts with more hydrated material. Furthermore, ordinary chondrite meteorite analogs (J. Grossman et al. 2000, R. Jones et al. 2014) and even samples returned from a similar L/LL type ordinary chondrite-like asteroid, Itokawa (Z. Jin and M. Bose 2019), show evidence of hydration among nominal anhydrous mineralogy.

Dinkinesh's 3-μm band appears deeper than the bands detected on several NEAs (some of which are similar size as Dinkinesh) and does not match any of the spectral shapes identified by L. McGraw et al. (2022). The Dinkinesh band also has no good matches among MBAs, being deeper than most of the 3-μm bands detected on larger S-complex MBAs (M. McAdam et al. 2024) but less deep than C-complex MBAs such as (24) Themis (A. Rivkin and J. Emery 2010) (Figure 7c). We again point out, however, that the depth and shape of the observed band may not be accurate due to the operating temperature issues described. While the details of the 3-μm band are uncertain, it is important to note that the 3-μm bands on Dinkinesh and Selam are indistinguishable from each other. This suggests that either the hydration is intimately integrated into the bulk composition of Dinkinesh, i.e. inherent or accumulated, likely via space weathering, since Selam was formed, which based on dynamic simulation is estimated to be ~1-10 Ma (H. Levison et al. 2024; C. Merrill et al. 2024). We are unable to distinguish between possible sources of the band on Dinkinesh.

6. Conclusions

L'Ralph in-flight performance has been stable to date. MVIC has shown good in-flight radiometric stability and its performance meets requirements in every channel with no major changes from ground calibration. LEISA's flight thermal performance has been better than expected, allowing for earlier calibration campaigns than originally planned. The LEISA radiometric calibration and pixel size have been updated since ground calibration using scans of Arcturus. Applying the new calibration to Dinkinesh flyby data show the asteroid spectra are in reasonable agreement with those of other S and Sq-type asteroids, with the presence of 1 and 2-μm pyroxene bands. Dinkinesh is spectrally, and likely mineralogically, similar to LL/L-type ordinary chondrite meteorites. We also show evidence for a 3-μm band, though calibration uncertainties limit its interpretation. Follow-up spectral observations (e.g., by James Webb Space Telescope) would be valuable for confirming and identifying the origin and significance of this band.

Calibration performance and trending work are ongoing and will include regular, brief, stellar and solar calibrations. A larger, comprehensive, calibration campaign is planned for when the spacecraft reaches 4 AU and instruments reach their full operating conditions, similar to those expected at the Trojans. These planned activities include a full radiometric calibration of L'Ralph using a range of standard stars. These future calibrations, as well as observations of the Main Belt asteroid (52246) Donaldjohanson in April 2025, may also facilitate future recalibration of the Dinkinesh data.

Acknowledgements

The authors thank the entire L'Ralph support teams for their continued support of the instrument even after launch, particularly the thermal team who correctly predicted the LEISA operating temperatures. The Lucy mission is funded through the NASA Discovery Program on contract No. NNM16AA08C. All calibrated L'Ralph data can be retrieved from

the PDS small bodies node at doi.org/10.26007/99kk-6s03 and doi.org/10.26007/f61e-0f52 (D. Reuter et al. 2024a; 2024b).

References:

Blank, R., Anglin, S., Beletic, J. et al. 2012. *Proceedings of SPIE Astronomical Telescopes + Instrumentation* 8453, 845310. DOI:10.1117/12.926752

Binzel, R.P., Rivkin, A.S., Bus, S.J., Sunshine, J.M., Burbine, T.H. 2001. *Meteoritics and Plan. Sci.* 36, 1167-1172. DOI: 10.1111/j.1945-5100.2001.tb01950.x

Binzel, R.P., Rivkin, A.S., Stuart, J.S. et al. 2004. *Icarus* 170, 259-295. DOI: 10.1016/j.icarus.2004.04.004

Binzel, R.P., DeMeo, F.E., Turtelboom, E.V., et al. 2019. *Icarus* 324, 41-76. DOI: 0.1016/j.icarus.2018.12.035

Bohlin, R.C., Gordon, K.D., Tremblay, P.-E. 2014. *PASP* 126, 711. DOI: 10.1086/677655

Bolin, B.T, Noll, K.S., Caiazzo, I., Fremling, C., Binzel, R.P. 2023. *Icarus* 400, 115562. DOI: 10.1016/j.icarus.2023.115562

Cloutis, E.A., Sanchez, J.A, Reddy, V., et al. 2015. *Icarus* 252, 39-82. DOI: j.icarus.2014.10.003

De Sanctis, M.C., Combe, J.P., Ammannito, E. et al. 2012. *ApJL* 758, L36. DOI: 10.1088/2041-8205/758/2/L36

Dunn, T.L, McCoy, T.J., Sunshine, J.M., McSween, H.Y. 2010. *Icarus* 208, 789-797. DOI: 10.1016/j.icarus.2010.02.016

Garrison, M., Reuter, D., Simon, A., et al. 2022. *Proceedings of 2022 IEEE Aerospace Conference.* DOI: 10.1109/AERO53065.2022.9843814

Grossman, J.N., Alexander, C.M., Wang. J., Brearley, A.J. 2000. Meteoritics and Planetary Science 35, 467-486. DOI: 10.1111/j.1945-5100.2000.tb01429.x

Gomez Barrientos, J., de Kleer, K., Ehlmann, B.L., et al. 2024. *ApJL* 967, L11. DOI: 10.3847/2041-8213/ad4647

Jones, R.H., McCubbin, F.M., Dreeland, L. et al. 2014. *Geochimica et Cosmochimica Acta* 132, 120-140. DOI: 10.1016/j.gca.2014.01.027

Labsphere 2017. Technical Guide: Integrating Sphere Theory and Applications. https://www.labsphere.com/wp-content/uploads/2021/09/Integrating-Sphere-Theory-and-Applications.pdf

Levison, H.F., Olkin, C.B., Noll, K.S., et al. 2021. *Planet. Sci. J.* 2,171. DOI: 10.3847/PSJ/abf840

Levison, H.F., Marchi, S., Noll, K.S., et al. 2024. *Nature* 629, 1015–1020. DOI: 10.1038/s41586-024-07378-0

Marsset, M., Vernazza, P., Broz, M. et al. 2024. *Nature*, submitted. DOI: arXiv:2403.08548

McAdam, M.M., Thomas, C.A., McGraw, L., Rivkin, A.S., Emery, J.P. 2024 *PSJ* submitted

McGraw, L.E., Emery, J.P., Thomas, C.A., et al. 2022. *Planet Sci. J.* 3, 243. DOI: 10.3847/PSJ/ac8ced

McGraw, L.E., Emery, J.P., Thomas, C.A., Rivkin, A.R. 2024. *Icarus* 422, 116252. DOI: 10.1016/j.icarus.2024.116252

McSween, H.Y., Bennett, M.E., Jarosewich, E. 1991. *Icarus* 90, 107-116. DOI: 10.1016/0019-1035(91)90072-2

Merrill, C.C., Kubas, A.R., Meyer, A.J., Raducan, S.D. 2024. *Astronomy & Astrophysics* 684, L20. DOI: 10.1051/0004-6361/202449716

Montanaro, M., Lunsford, A., Tesfaye, Z., Wenny, B., Reuter, D. 2014. *Remote Sensing* 6, 8803-8821. DOI: 10.3390/rs6098803

Olkin, C.B., Levison, H.F., Vincent, M., et al. 2021. *Planet. Sci. J.* 2, 172. DOI: 10.3847/PSJ/abf83f

Olkin, C.B., Vincent, M., Adam, C., et al. 2024. *Space Sci. Rev*. 220, 47. DOI: 10.1007/s11214-024-01082-1

Pearlman, A., Montanaro, M., Efremova, B., et al. 2020. *IEEE Transactions on Geoscience and Remote Sensing* 59, 2715-2726. DOI: 10.1109/TGRS.2020.3008655

Polishook, D., DeMeo, F.E., Burt, B.J., et al. 2023. *Planet. Sci. J*. 4, 229. DOI: 10.3847/PSJ/ad08ae

Rayner, J.T., Cushing, M.C., Vacca, W.D. 2009. *Astrophysical Journal Supplement Series* 185, 289. DOI: 10.1088/0067-0049/185/2/289

Reuter, D.C., Stern, S.A., Scherrer, J., et al. 2008. *Space Sci. Rev*. 140, 129-154. DOI: 10.1007/s11214-008-9375-7

Reuter, D.C., Simon, A.A., Hair, J., et al. 2018. *Space Sci. Rev*. 214, 54. DOI: 10.1007/s11214-018-0482-9

Reuter, D.C., Simon, A.A., Lunsford, A., et al. 2023. *Space Sci. Rev*. 219, 69. DOI: 10.1007/s11214-023-01009-2

Reuter, D., Simon, A., Lunsford, A., Kaplan, H., Grundy, W., Howett, C., Montanaro, M., Weigle, G. 2024a. Lucy L'Ralph LEISA Dinkinesh Calibrated Data Collection, urn:nasa:pds:lucy.leisa:data_dinkinesh_calibrated::1.0, D. Kaufmann, M. K. Crombie, C. Gobat, and J. W. Parker (eds.), NASA Planetary Data System. DOI: 10.26007/99kk-6s03

Reuter, D., Simon, A., Lunsford, A., Kaplan, H., Grundy, W., Howett, C., Montanaro, M., Weigle, G. 2024b. Lucy L'Ralph MVIC Dinkinesh Calibrated Data Collection, urn:nasa:pds:lucy.mvic:data_dinkinesh_calibrated::1.0, D. Kaufmann, M. K. Crombie, C. Gobat, and J. Wm. Parker (eds.), NASA Planetary Data System. DOI: 10.26007/f61e-0f52

Rivkin, A.S., Emery, J.P. 2010. *Nature* 464, 1322–1323. DOI: 10.1038/nature09028

Rivkin, A.S., Howell, E.S., Emery, J.P., Sunshine, J. 2018. *Icarus* 304, 74-82. 10.1016/j.icarus.2017.04.006

Simon, A.A., Reuter, D.C., Gorius, N., et al. 2018. *Remote Sensing* 10, 1486. DOI: 10.3390/rs10091486

Simon, A.A., Reuter, D.C., Lauretta, D.S. 2021. *J. Astron. Telesc. Instrum. Syst*. 7, 020501. DOI: 10.1117/1.JATIS.7.2.020501

Spencer, J.R., Bell, J.F, Christensen, P.R., et al. 2024. *Space Sci. Rev*. 220, 3. DOI: 10.1007/s11214-023-01034-1

Sunshine, J.M., Farnham, T.L., Feaga, L.M., et al. 2009. *Science* 326, 565-568. DOI: 10.1126/science.1179788

Vernazza, P., Zanda, B., Binzel, R.P. et al. 2014. *ApJ* 791, 120. DOI: 10.1088/0004-637X/791/2/120

Zin, J., Bose, M. 2019. *Science Advances* 5, eaav8106. DOI: 10.1126/sciadv.aav8106

638 Table 1. L'Ralph Dinkinesh observations

Time	Scan	Phase Angle Start (°)	Phase Angle End (°)	Range Start (km)	Range End (km)	Frame Rate (ms)	MVIC TDI per band
-368 s	MVIC Approach	104		1700		7.2	4, 8, 8, 8, 8, 8
-289 s	LEISA Approach	101	90	1372	897	80	
-55 s	MVIC C/A	60	58	485		7.2	4, 4, 4, 4, 4, 8
+92 s	LEISA C/A	16	31	614	860	70	
+250 s	MVIC Departure	40		1215		7.2	4, 4, 4, 4, 4, 8
+337 s	LEISA Departure	46	49	1675	2033	75	

639

640

641 Table 2. Dinkinesh wavelength fits for the 1.5-μm peak and the 2-μm absorption.

	1.5-μm peak center (μm)	2-μm band center (μm)
Close Approach	1.51 ± 0.02	1.95 ± 0.02
Departure	1.52 ± 0.02	1.94 ± 0.06

642

643

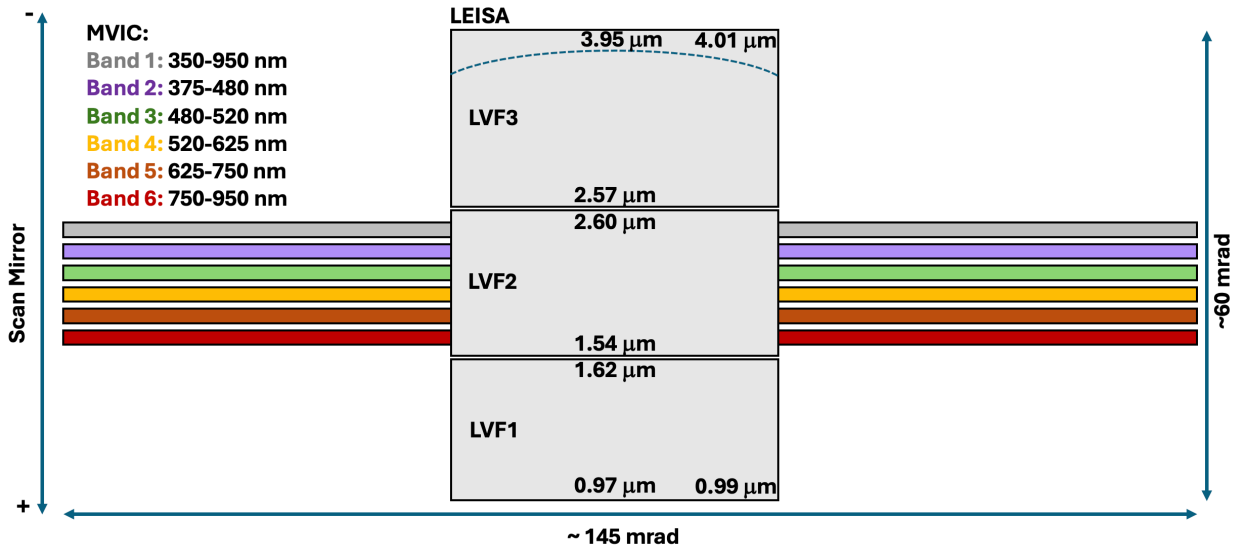

Figure 1. The L'Ralph focal planes to scale. LEISA and MVIC share the same optical path but have different fields of view and spatial resolutions. The instrument scan mirror is used to scan a target across the MVIC or LEISA filters to build up spectral image cubes.

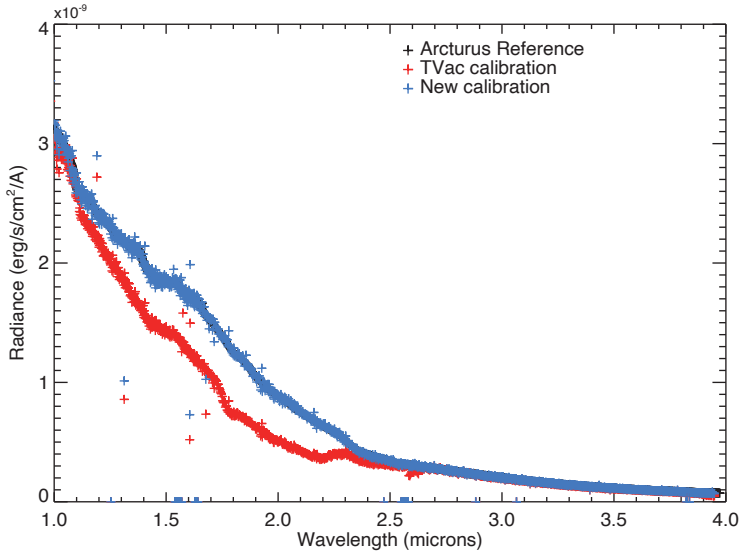

Figure 2. LEISA Arcturus calibration. The LEISA stellar scans were used to compare calibrated radiance with an Arcturus reference spectrum; the calibration coefficients from TVac (red points) were adjusted (blue points) to match the known radiance.

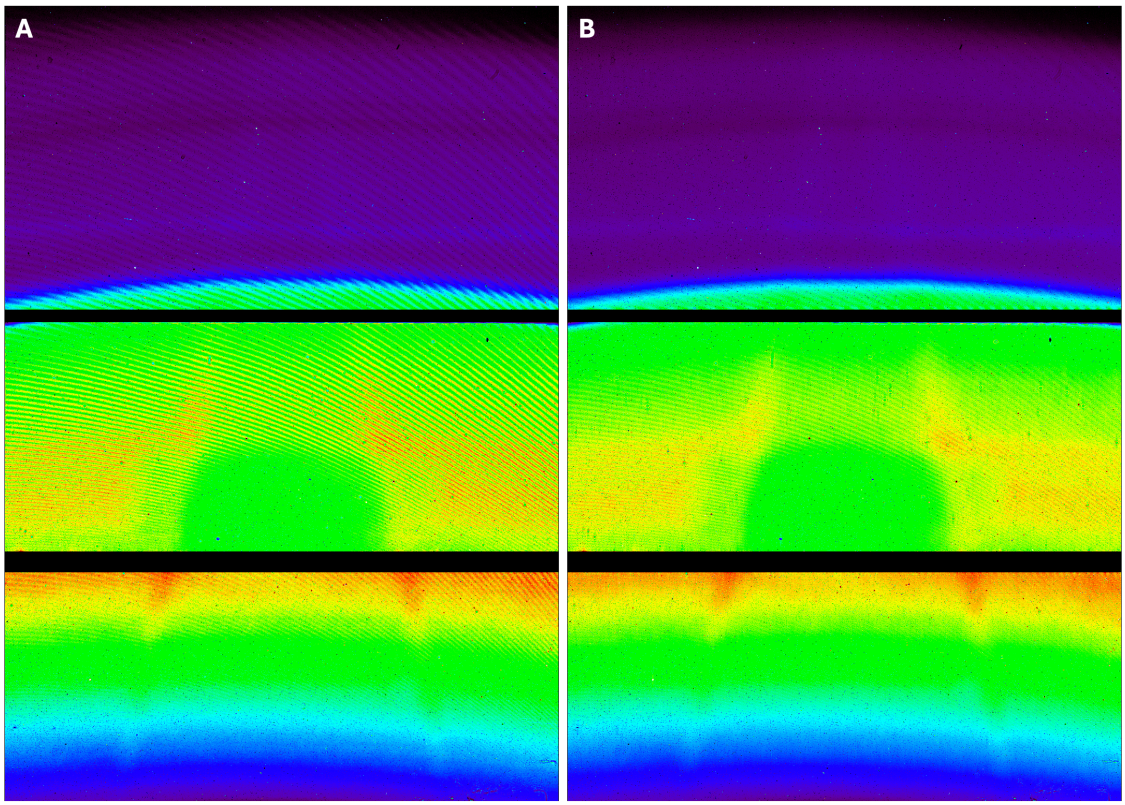

Figure 3. LEISA optical fringes in calibration data. For both frames, the long wavelength end is at the top, short wavelength end at the bottom. The round feature near the center is caused by the calibrator scatter plate and the inverted V-shaped feature across the bottom filters is from reflections off the cold snout surrounding LEISA. A) Internal filament calibrator data show significant optical fringing apparent as higher frequency diagonal lines. B) Fringing is greatly reduced after applying a fringe flat correction.

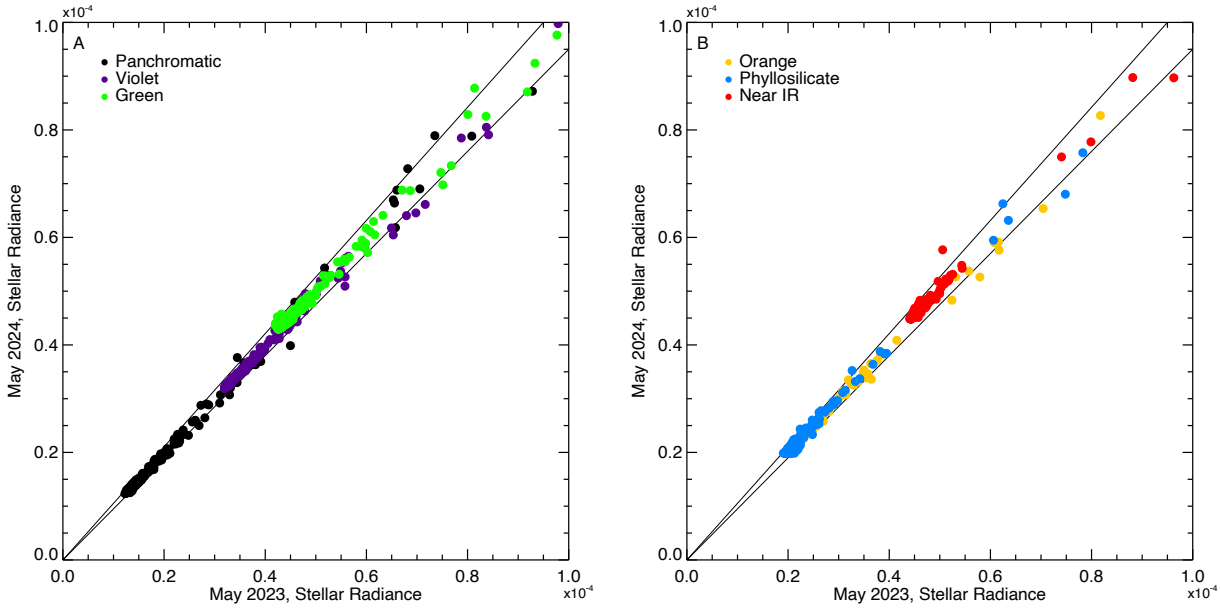

Figure 4. MVIC stellar calibrations from March 2023 and March 2024. A) Panchromatic, Violet, and Green channels and B) Orange, Phyllosilicate, and Near-IR channels. Stars were chosen separately for each channel based on signal level, and all bands show stable radiometric performance ±5% over that time period.

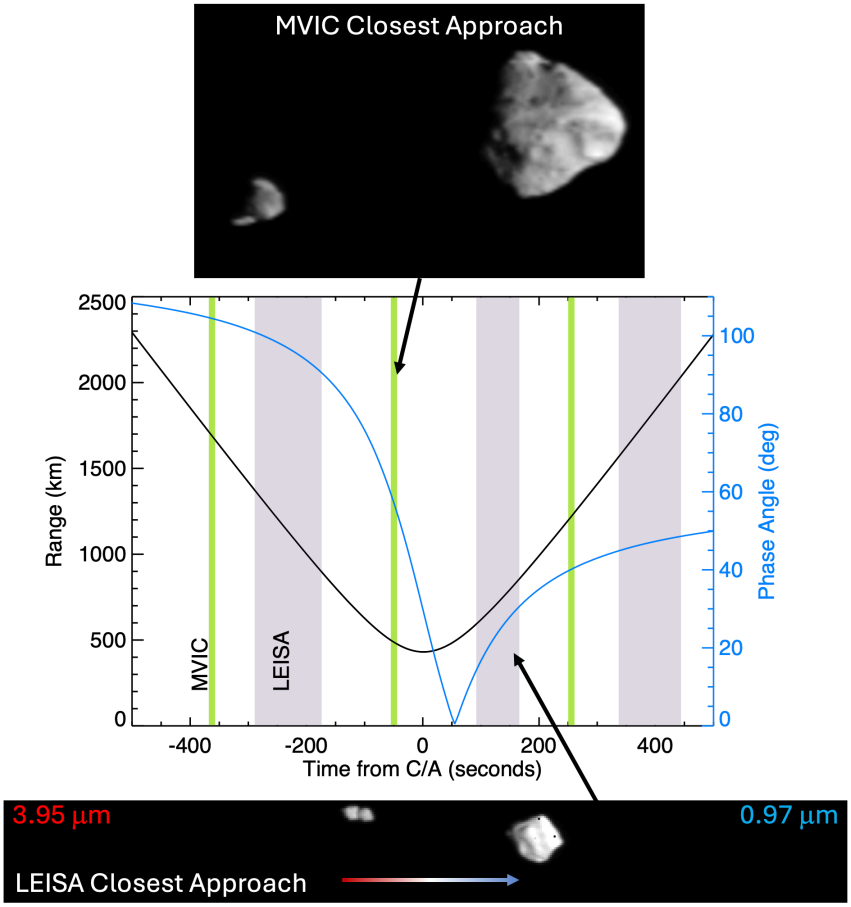

669

670 Figure 5. Dinkinesh closest approach views from MVIC and LEISA. The top image is the
671 MVIC pan band image showing Dinkinesh (right) and Selam (left), while the bottom image
672 shows a single frame acquired near the center of the LEISA scan. The central plot shows
673 the changing range and phase angles during each of the LEISA and MVIC observations.

674

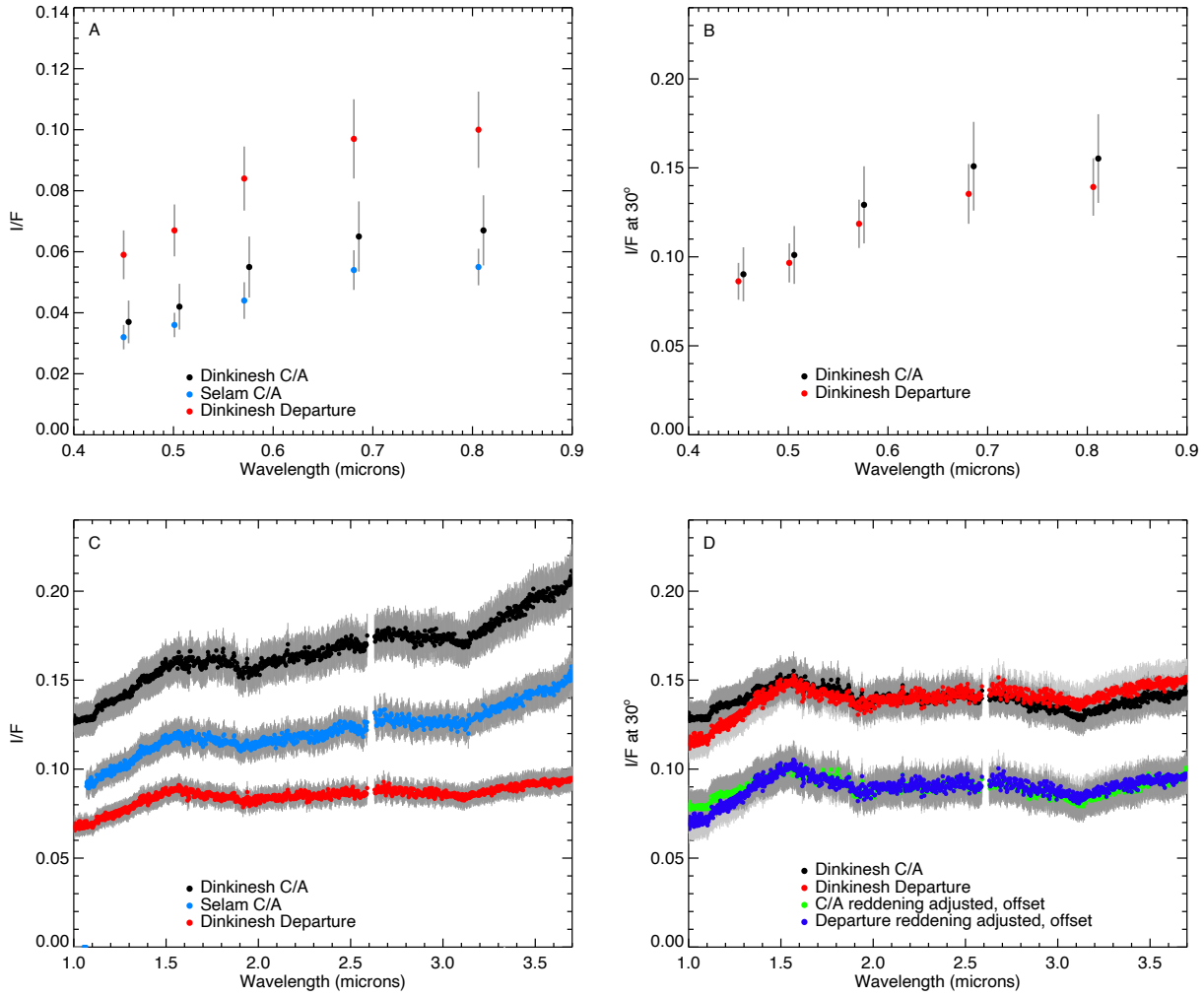

675

676 Figure 6. Spectra of Dinkinesh and Selam. A) MVIC *I/F* for Dinkinesh closest approach (red)
677 and at lower phase on departure (black). Selam is shown at closest approach and has a
678 similar spectral shape to Dinkinesh (blue). B) Simultaneously fit MVIC *I/F* scans phase
679 corrected to 30°. C) LEISA Dinkinesh spectrum from closest approach (black) and at higher
680 phase on departure (red). Selam at closest approach again shows a nearly identical
681 spectral shape to Dinkinesh. D) Simultaneously fit LEISA scans phase corrected to 30° and
682 with a phase reddening correction.

683

684

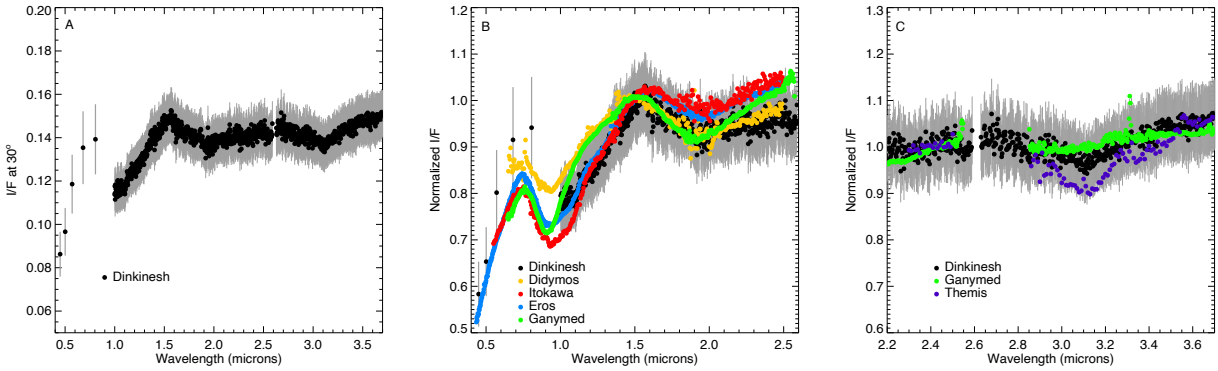

Figure 7. Dinkinesh spectral comparisons. A) The composite MVIC and LEISA departure scan Dinkinesh data corrected to 30° phase. B) The short wavelength spectrum, normalized at 1.5 μm, with comparisons to other S and Sq-type asteroid spectra (R. Binzel et al. 2001, 2004, L. McGraw et al. 2022, D. Polishook et al. 2023). C) Dinkinesh's 3-μm absorption band, normalized at 2.9 μm, compared with that of Ganymed and Themis (A. Rivkin & J. Emery 2010, L. McGraw et al. 2022).

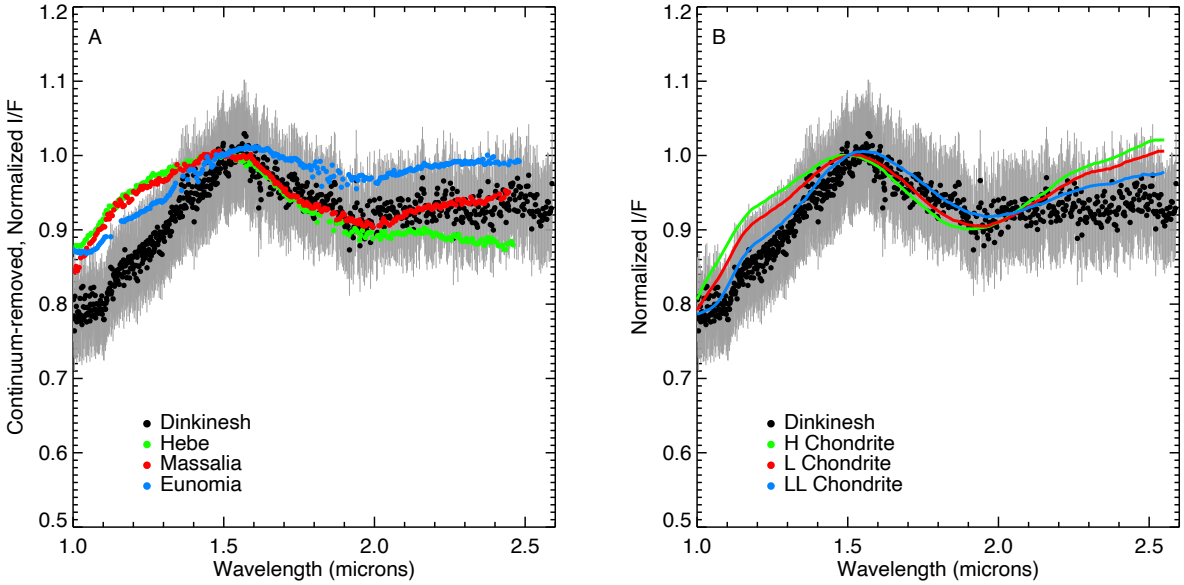

Figure 8. Comparison of Dinkinesh with representative asteroids and their corresponding chondrites. A) Dinkinesh's spectrum (black points), continuum-removed and normalized at 1.5 μm, compared with those of Hebe, Massalia, and Eunomia (R. Binzel et al. 2019). B) The

same comparison, but with average ordinary chondrite sub-type spectra (T. Dunn et al. 2010).

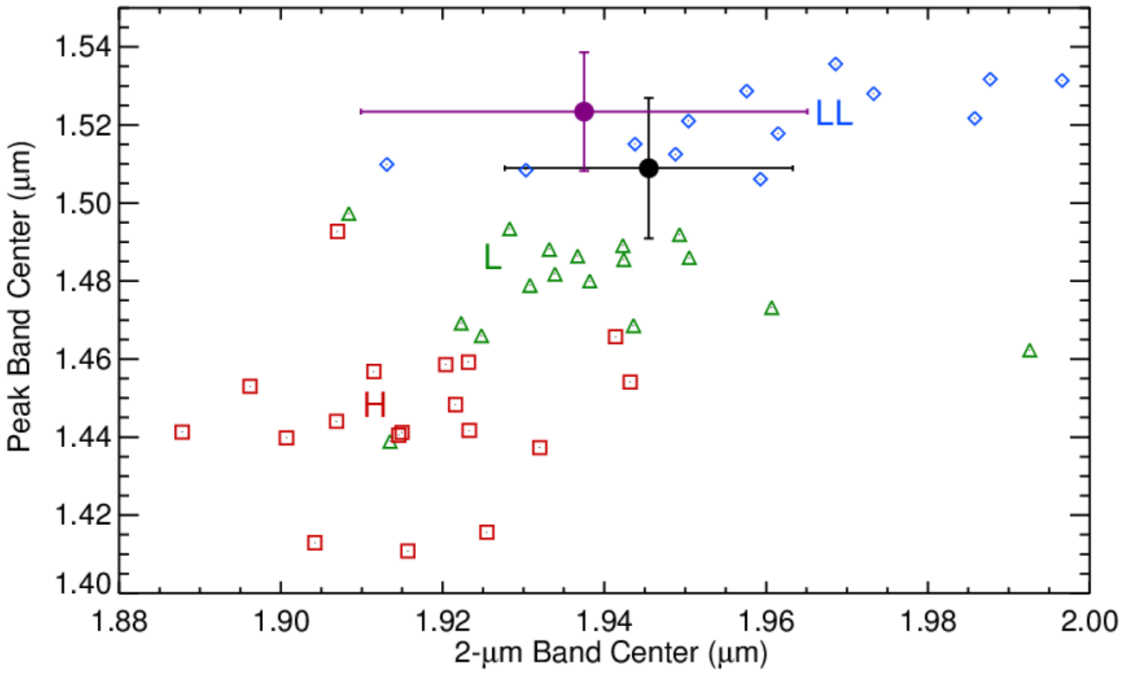

Figure 9. Locations of the centers of the 1.5-µm peak and 2-µm absorption in LL (blue diamonds), L (green triangles), and H (red squares) ordinary chondrites. These ordinary chondrite sub-types are distinguishable in this parameter space. The measured parameters for the Dinkinesh spectra (filled circles – black is the close approach spectrum and magenta is the departure spectrum) are shown to agree with LL and L chondrites.